Optical Fiber Technology **5,** 363–389 (1999)
Article ID ofte.1999.0306, available online at http://www.idealibrary.com on IDEAL®

Invited Paper

An Efficient Simulation Model of the Erbium-Doped Fiber for the Study of Multiwavelength Optical Networks*

I. Roudas†

Corning, Inc., 2200 Cottontail Lane, Somerset, New Jersey 08873

D. H. Richards

Bell Communications Research, 331 Newman Springs Road, Red Bank, New Jersey 07701

N. Antoniades‡

Corning, Inc., 2200 Cottontail Lane, Somerset, New Jersey 08873

J. L. Jackel

Bell Communications Research, 331 Newman Springs Road, Red Bank, New Jersey 07701

and

R. E. Wagner†

Corning, Inc., Corning, New York 14831

Received March 3, 1999

The first part of this paper reviews the spectrally resolved erbium-doped fiber model by Saleh, Jopson et al. (1990, *IEEE Photon Technol. Lett.* **2**, 714; 1991, Fiber Laser Sources and Amplifiers III, Vol. 1851, pp. 114–119, SPIE). This model is adequate for fast simulation of erbium-doped fiber amplifiers

* This work was performed as a part of the MONET consortium under DARPA funding agreement MDA 972-95-3-0027.

† Previously with Bell Communications Research.

‡ Previously with the Center for Telecommunications Research, Department of Electrical Engineering, Columbia University, 530W. 120th St., Schapiro Research Building, New York, NY 10027.

1068-5200/99 $30.00

pumped at 980 or 1480 nm which are not self-saturated by amplified spontaneous emission noise. The second part of this paper reviews the wavelength-domain representation of optical signals and network components at the optical transport layer of multiwavelength optical networks. This representation stems from the spectrally resolved model of erbium-doped fiber amplifiers. Optical signals are represented by their carrier wavelength and average power exclusively and not by their temporal waveform, as is customary in simulation of analog and digital communication systems. In addition, network components are fully characterized by their loss or gain as a function of wavelength. The wavelength-domain representation is adequate for efficient steady-state and transient power-budget computations; i.e., it can be used to evaluate the optical signal, amplified spontaneous emission noise, and linear optical crosstalk average powers at all points in a multiwavelength optical network. To illustrate the capabilities of the spectrally resolved erbium-doped fiber model by Saleh, Jopson et al. and the wavelength-domain representation, transient power fluctuations caused by the dynamic interaction of saturated erbium-doped fiber amplifiers and servo-controlled attenuators in a bidirectional ring composed of four wavelength add–drop multiplexers are studied. The mechanisms responsible for this oscillatory behavior are identified and remedies are proposed.

I. INTRODUCTION

The rapid growth and the future commercial importance of multiwavelength optical networking create strong incentives for the development of efficient software tools for the design of the optical transport layer [3, pp. 580–581].

The choice of the model of erbium-doped fiber amplifiers (EDFAs) is a key issue for the efficient performance evaluation of multiwavelength optical networks because EDFAs are an essential part of most network elements. Accurate EDFA modeling presents a high degree of computational complexity [3, chap. 1; 4]. To reduce computation time, several approximate models are proposed in the literature, e.g., [1–17].

The first part of this paper reviews the spectrally resolved erbium-doped fiber (EDF) model by Saleh, Jopson et al. [1, 2]. This model is adequate for simulation of EDFAs pumped at 980 or 1480 nm which are not self-saturated by amplified spontaneous emission (ASE) noise. The model can compute the gain and ASE noise of EDF based on the numerical solution of a small number of transcendental equations. The formalism for the evaluation of EDF gain has been extensively presented before [1–10, 12] and is briefly summarized here for the sake of completeness. The method for the evaluation of EDF ASE noise was presented before only in Refs. [2, 12] and is analyzed here in more depth. In particular, the implications of the deliberate nonconservation of particles of this model are investigated. The paper also discusses a variant extending the validity of the basic steady-state model to the ASE self-saturation regime [12]. Finally, emphasis is given to issues related to the numerical solution of the transcendental equations and to the importance of the initial guess of the solution for the speed of calculation and potential overflow.

For the study of large-scale networks with a large number of wavelengths, it is also necessary to adopt a simplified representation of the optical signals and network components. The second part of this paper reviews the key concepts of the wavelength-domain representation of optical signals in the optical transport layer [18]. According to this method, optical signals are represented by their carrier wavelength and average power exclusively and not by their temporal waveform, as is customary in simulation of analog and digital communication systems [19]. In addition, the constituent parts of the network are fully characterized by their loss or gain as a function of wavelength.

This representation is similar to that of an optical spectrum analyzer and is an extension of the spectrally resolved EDF model to other transparent network element components. The term ''wavelength-domain'' implies a coarse resolution bandwidth compared to the frequency-domain representation used in waveform-level simulation. The wavelength-domain representation is adequate for the study of power-budget related problems in transparent optical networks.

A general purpose simulation tool for both steady-state and transient analysis was implemented based on this representation [18] in the context of the multiwavelength optical networking (MONET) project [20]. This tool can be used to compute the optical signal, ASE noise, and linear optical crosstalk power spectra at all points in the network. The system performance can be evaluated in terms of optical signal-to-noise ratio (SNR). In addition, information provided by wavelength-domain simulation can be used to simplify and accelerate waveform level simulations [18].

In this article we give an example of effective use of the wavelength-domain simulation in the study of transient effects due to abrupt changes of the signal power levels (i.e., during network reconfiguration, failures, protection switching, and so forth) in a bidirectional multiwavelength optical ring topology. It is shown that wavelength-domain simulation can be a very powerful tool to address power-budget related problems in multiwavelength optical networks.

The rest of the paper is organized as follows: Section II reviews the accurate homogeneous two-level EDF model and explains in detail its approximate solution in the steady-state regime by Saleh, Jopson et al. [1, 2]. In addition, this section shows that the model in Refs. [1, 2] does not conserve the number of particles and presents variants that correct this flaw. Section III describes the operation principles of wavelength-domain simulation. Section IV presents sample simulation results for the transient power fluctuations in a bidirectional wavelength add−drop multiplexer (WADM) optical ring network caused by the dynamic interaction of servo-controlled attenuators and saturated EDFAs. In the Appendix, the servo-controlled attenuator model used in the simulations is presented and analyzed.

II. EDF MODEL

In this section, the EDF model presented in Refs. [1, 2] is reviewed. The complete homogeneous two-level EDF model [3, chap. 1; 4] is used as a starting point. Then the model in Refs. [1, 2] is derived and analyzed incorporating elements of the most recent literature.

A. Homogeneous Two-Level EDF Model

In the following, all optical powers are expressed in photons/s.

Consider a strand of EDF of length L. An arbitrary number M of optical beams of carrier wavelength λ_k and average input power P_k^{in}, $1 \leq k \leq M$, enter the EDF and propagate along the fiber axis (z-axis), either in the forward (positive z) or backward (negative z) direction. These beams can represent signals, pumps, or ASE noise coming from the modules surrounding the EDF and their wavelengths λ_k, $1 \leq k \leq M$ are not necessarily distinct. The ASE noise power spectrum generated in the EDF covers a continuum of wavelengths but for simulation purposes the wavelength axis is discretized in N wavelength bins. The forward and backward ASE noise are represented by N optical beams with carrier wavelengths λ_l, bandwidths $\Delta\nu_l$ centered around λ_l, and average powers denoted by $P_{n,l}^{\pm}(z,t)$, $1 \leq l \leq N$, where the superscript $\pm$ indicates forward $(+)$ or backward $(-)$ direction of propagation. In general, $M \neq N$. Without loss of generality, the wavelengths of the M input optical beams are assumed to coincide exactly with some of the N nodes of the wavelength grid used for the discretization of the ASE noise generated internally in the EDF, i.e., λ_k, $1 \leq k \leq M$ is a subset of λ_l, $1 \leq l \leq N$.

Common modeling assumptions are summarized in [3, chap. 1; 4, 7]: under 1480 or 980 nm pumping with pump power less than about 1 W [4], the erbium ions can populate two atomic energy levels (referred to as a two-level model); the permanent electric field in the glass host induces Stark-splitting of these atomic energy levels but atomic transitions can still be described by a two-level model due to fast thermalization of the manifolds; inhomogeneous broadening [3, chap. 1], temperature dependence of the absorption and emission spectra [4], excited state absorption, upconversion [21, 22], Rayleigh scattering [23–25], background loss, and polarization effects [24, 26, 27] are neglected. In addition, following the description of [4], the erbium ion distribution is assumed radially symmetric and confined to the center of the transversal electric field of the optical signals. The populations of the erbium ions in the ground and upper state are denoted by $N_1(z,t)$, $N_2(z,t)$, respectively, and they are normalized to the peak erbium ion density ρ so that $N_1(z,t) + N_2(z,t) = 1$. In this case $N_1(z,t)$, $N_2(z,t)$ represent average values obtained by integration over the transverse plane [4].

Based on the above assumptions, a semi-classical phenomenological model is derived [3, chap. 1; 4]. A rate equation describes the decay rate of the fractional population of the erbium ions in the upper state $N_2(z,t)$ as a function of the total powers $P_k^{tot}(z,t)$ at each point z in the EDF. In addition, $M + 2N$ partial differential equations describe the rate of change of the average power $P_k(z,t)$ of the input optical beams and of the forward and backward ASE noise $P_{n,l}^{\{\pm\}}(z,t)$ during propagation due to the interaction between the light beams and the erbium ions. The model is summarized by the following set of coupled nonlinear partial differential equations (PDEs) [3, chap. 1; 4]:

$$\frac{\partial N_2(z,t)}{\partial t} = -\frac{1}{\rho A}\sum_{k=1}^{N}\left[\gamma_k N_2(z,t) - \alpha_k N_1(z,t)\right]P_k^{tot}(z,t) - \frac{N_2(z,t)}{\tau} \tag{1}$$

$$u_k \frac{\partial P_k(z,t)}{\partial z} = \left[\gamma_k N_2(z,t) - \alpha_k N_1(z,t)\right]P_k(z,t) \qquad 1 \le k \le M \tag{2}$$

$$u_l \frac{\partial P_{n,l}^{\{\pm\}}(z,t)}{\partial z} = \left[\gamma_l N_2(z,t) - \alpha_l N_1(z,t)\right]P_{n,l}^{\{\pm\}}(z,t) + P_{0,l}(z,t)\gamma_l N_2(z,t) \qquad 1 \le l \le N \tag{3}$$

where ρ is the peak erbium ion density, A is the effective doping area, u_k, u_l are propagation-indicating flags taking the value $+1$ for forward propagating beams and -1 for backward propagating beams, τ is the fluorescence lifetime of the upper level, α_k and γ_k are the absorption and emission coefficients at wavelength λ_k, respectively, $P_{0,l} = 2\Delta\nu_l$ is the average power of the initial spontaneous emission noise at point z in the fiber, and $P_k^{tot}(z,t)$ is given by $P_k^{tot}(z,t) = P_k(z,t) + P_{n,k}^{+}(z,t) + P_{n,k}^{-}(z,t)$.

This set of coupled nonlinear PDEs (1)–(3) can be solved numerically [28]. A discussion about the adequacy of different numerical methods was given in [3, chap. 1]. The convergence of the numerical methods depends on the initial guess of boundary conditions, pumping configuration, and input powers. Techniques to facilitate convergence were proposed in [29]. In any case, integration over fiber length and time makes any numerical procedure computationally intensive. Techniques to reduce the number of PDEs in (1)–(3) and speed-up calculations by using nonuniform sampling of the ASE spectrum were proposed in [4, 30, 31]. In addition, a number of simplified models were proposed in the literature [1–17]. Here, we limit our interest to the simplified EDF model of Refs. [1, 2].

B. Steady-State Noise-Free EDF Model [1]

In low-gain strongly saturated EDFAs, ASE noise can be neglected in a first approach. In this case, by setting in (1) the time derivative equal to zero, combining (1), (2), and integrating over the entire fiber length, it can be shown that input and output optical powers in the EDF are related by the following set of equations [1]:

$$P_k^{out} = P_k^{in} e^{-\alpha_k L} e^{(P_{in} - P_{out})/P_k^{IS}} \qquad 1 \le k \le M, \tag{4}$$

where P_k^{in}, P_k^{out} are the input and output optical powers, respectively, at wavelength λ_k, P_k^{IS} is the intrinsic saturation power at λ_k defined as $P_k^{IS} \triangleq \zeta/(\alpha_k + \gamma_k)$, where ζ is the fiber saturation parameter defined as $\zeta \triangleq \rho A/\tau$, and P_{in} and P_{out}

are the total input and output powers, respectively:

$$P_{in} = \sum_{j=1}^{M} P_j^{in} \tag{5}$$

$$P_{out} = \sum_{j=1}^{M} P_j^{out}. \tag{6}$$

It is worth noting that Eqs. (4) are valid both for forward and backward propagating signals.

Relations (4) define a nonlinear set of equations. By summing over k, the set of equations (4) can be reduced to a single transcendental equation;

$$P_{out} = \sum_{k=1}^{M} A_k e^{-B_k P_{out}}, \tag{7}$$

where now A_k, B_k are defined as follows:

$$A_k = P_k^{in} e^{-\alpha_k L} e^{P_{in}/P_k^{IS}} \tag{8}$$

$$B_k = \frac{1}{P_k^{IS}}. \tag{9}$$

Since A_k, B_k are known, Eq. (7) can be solved numerically (see subsection II-F). Once P_{out} is known, P_k^{out} can be calculated by substitution in (4).

C. Steady-State Refined EDF Model with ASE Noise [2]

In the above steady-state noise-free EDF model, ASE noise generated in the EDF can be added a posteriori [2]. The ASE noise power is evaluated by resolution of the set of ordinary differential equations (3):

$$u_l \frac{dP_{n,l}^{\{\pm\}}(z)}{dz} = \left[\gamma_l N_2(z) - \alpha_l N_1(z)\right] P_{n,l}^{\{\pm\}}(z) + P_{0,l}\gamma_l N_2(z) \qquad 1 \le l \le N. \tag{10}$$

It is assumed that $N_1(z), N_2(z)$ are functions of the signal powers $P_k(z)$, $1 \le k \le M$ only and do not depend on the ASE noise powers $P_{n,l}^{\{\pm\}}(z)$, $1 \le l \le N$ (i.e., there is no ASE noise self-saturation). Then each equation of the above set (10) is a first order linear ordinary differential equation that can be solved independently and exactly using integrating factors [32]. The ASE noise powers are given by

$$P_{n,l}^{+}(L) = \int_0^L dP_l(z) G_l^{+}(z, L) \tag{11}$$

$$P_{n,l}^{-}(0) = \int_0^L dP_l(z) G_l^{-}(0, z), \tag{12}$$

where we made use of the notation of [2]

$$dP_l(z) = P_{0,l}\gamma_l N_2(z)\, dz \tag{13}$$

$$G_l^+(z, L) = \exp\left\{\int_z^L [\gamma_l N_2(x) - \alpha_l N_1(x)]\, dx\right\} \tag{14}$$

$$G_l^-(0, z) = \exp\left\{\int_0^z [\gamma_l N_2(x) - \alpha_l N_1(x)]\, dx\right\}. \tag{15}$$

In the above, $dP_l(z)$ is the power of the ASE noise generated in an infinitesimal EDF segment of length dz centered around point z, and $G_l^+(z, L)$ and $G_l^-(0, z)$ are the gain coefficients for the fiber segments $[z, L]$ and $[0, z]$ for forward and backward propagating signals, respectively.

For the evaluation of integrals (11), (12), it is necessary to compute the fractional upper state population $N_2(z)$ and the gain coefficients $G_l^+(z, L)$ and $G_l^-(0, z)$.

Setting in (1) the time derivative equal to zero and replacing $N_1(z, t) = N_1(z) = 1 - N_2(z)$, the fractional upper state population $N_2(z)$ can be expressed as an explicit function of the total powers $P_k^{tot}(z)$ at each point z in the EDF,

$$N_2(z) = \frac{\sum_{k=1}^N \alpha_k P_k^{tot}(z)}{\zeta\left[1 + \sum_{k=1}^N P_k^{tot}(z)/P_k^{IS}\right]} \simeq \frac{\sum_{k=1}^M \alpha_k P_k(z)}{\zeta\left[1 + \sum_{k=1}^M P_k(z)/P_k^{IS}\right]}, \tag{16}$$

where it is assumed that ASE noise self-saturation is negligible so $P_k^{tot}(z) \simeq P_k(z)$, $1 \le k \le M$.

For the calculation of (16) it is necessary to compute the powers $P_k(z)$ at each point z in the EDF. This can be done using the set of equations (4). We observe that relations (4) for a length of fiber z can be rewritten in the form

$$P_k(z) = P_k(0)e^{-u_k\alpha_k z}e^{u_k[S(0)-S(z)]/P_k^{IS}} \qquad 1 \le k \le M, \tag{17}$$

where

$$S(z) \triangleq \sum_{k=1}^M u_k P_k(z). \tag{18}$$

By multiplying both members with the propagation indicating flags u_k and summing over k, the set of equations (17) can be reduced to a single transcendental equation similar to Eq. (7),

$$S(z) = \sum_{k=1}^M C_k(z)e^{-u_k B_k S(z)}, \tag{19}$$

where we defined the auxiliary variables

$$C_k = u_k P_k(0)e^{-u_k\alpha_k z}e^{u_k B_k S(0)}. \tag{20}$$

The transcendental equation (19) can be solved numerically (see subsection II-F). Once $S(z)$ is known, $P_k(z)$ can be computed by substitution in (17). Then Eq. (16) can be calculated.

Finally, from (17) it is straightforward to show that the gain coefficients (14), (15) can be calculated by

$$G_l^+(z, L) = e^{-\alpha_l(L-z)} e^{[S(z)-S(L)]/P_l^{IS}} \tag{21}$$

$$G_l^-(0, z) = e^{-\alpha_l z} e^{[S(0)-S(z)]/P_l^{IS}}. \tag{22}$$

Once $N_2(z,t), G_l^+(z,L), G_l^-(0,z)$ are known, integrals (11), (12) are computed numerically (see subsection II-F).

The major advantage of the model by Saleh, Jopson et al. [1, 2] is the high execution speed compared to the numerical solution of (1)–(3). Another advantage of this model is that it requires only a small number of parameters a_k, P_k^{IS}, L which can be easily measured [1, 2]. All other parameters of the model can be derived by the above measurements.

The model can be extended to take into account arbitrary mode field profiles and dopant distributions [4, 5], ASE self-saturation [3, pp. 379–382; 12], transient effects [7–10], or other rare-earth-doped fibers [33].

D. Nonconservation of Particles

In this subsection, it is shown that the major implication of neglecting the ASE noise self-saturation in the derivation of relations (4), (11), (12), (16), (17), (21), (22) is that the number of particles in the EDF model by Saleh, Jopson et al. [1, 2] is not conserved. The gain and consequently the output power of the signals and the ASE noise are larger than in reality. The error increases with the EDF gain. In high gain EDFs, this leads to dramatically false results.

Adding (2), (3), substituting in (1), and integrating over the fiber length L, it is straightforward to derive the following accurate relation for the conservation of particles, which is similar to the expression (7) in [34],

$$\begin{aligned} \frac{\partial r(t)}{\partial t} = & \sum_{k=1}^{M} \left[P_k^{in}(t) - P_k^{out}(t) \right] - \sum_{l=1}^{N} \left[P_{n,l}^{+}(L,t) + P_{n,l}^{-}(0,t) \right] \\ & - \frac{r(t)}{\tau} \left[1 - 2 \sum_{l=1}^{N} \frac{\gamma_l}{\gamma_l + \alpha_l} \frac{P_{0,l}}{P_l^{IS}} \right], \end{aligned} \tag{23}$$

where $r(t) = \rho A \int_0^L N_2(z,t)\,dz$ is the total number of the Erbium ions at the upper state (also referred to as *reservoir* [10]). The sum in the last term in the right hand side of (23) represents the spontaneously emitted photons that are guided.

Assuming ASE noise is negligible, then relations (3) can be ignored and, following a similar procedure as above, it is straightforward to derive the following approximate relation for the conservation of particles, which is the same as the expression (24) in [7] or expression (4) in [10]:

$$\frac{\partial r(t)}{\partial t} = \sum_{k=1}^{M} \left[P_k^{in}(t) - P_k^{out}(t) \right] - \frac{r(t)}{\tau}. \tag{24}$$

Obviously, the approximate expression (24) can be also derived from the relation (23) by setting the term representing the spontaneously emitted photons that are guided as well as the ASE noise terms $P_{n,l}^{+}(L,t)$, $P_{n,l}^{-}(0,t)$ to zero.

By comparison of (23), (24) the physical meaning of the approximations in the model presented in Refs. [1, 2] is revealed. All available input photons are exchanged between the input signals and the pump. The output photons of the ASE noise as evaluated by (11), (12) are not included in the approximate conservation equation (24). This is a consequence of the assumption that the ASE self-saturation is negligible. In addition, a fictitious number of ASE noise photons is added at the output by (11), (12). The violation of the conservation of particles is the reason that the model in Refs. [1, 2] fails to describe high gain EDFs (e.g., in preamplifiers). Variants of the model in Refs. [1, 2] that correct this flaw exist [3, pp. 379–382; 12]. The latter is the most accurate and is examined in detail below.

E. Extension to the Steady-State ASE Self-Saturated Regime

A variant of the model by Saleh and co-workers [1, 2] which is adequate for ASE self-saturated EDFAs was proposed initially by [2] and examined in detail by [12]. It consists of dividing a long ASE noise self-saturated EDF into shorter segments that are not ASE noise self-saturated and applying the model of subsection II-C to each segment. The output signals from each EDF segment are used as feedback input signals to the adjacent EDF segments. Several iterations must be performed to achieve convergence. By increasing the number of segments, the accuracy at the evaluation of ASE noise increases at the expense of efficiency.

The drawback of the model by [12] is that the number of operations that are necessary to compute the EDF gain increases nonlinearly with the number of segments. The reason for this increase is two-fold: first, dividing the EDF into K segments is like cascading K EDFs in the place of one so the number of operations increases by a factor K; second, due to the feedback from adjacent segments, one needs several iterations to achieve convergence. The number of iterations increases with the number of segments. The execution time is estimated by [12] to increase by at least a factor of $10K$ compared to the basic ASE noise model by [2]. In all cases studied by the present authors, the execution time required by the model of [12] even for $K = 2$ was comparable to the execution time required for the full numerical solution of (1)–(3) to achieve the same accuracy. Therefore, the practical value of this model remains ambiguous.

Apart from the variants by [3, pp. 379–382; 12], a number of alternative EDF models were proposed for the modeling of ASE noise self-saturated EDFAs [11, 13–17]. A comparison of these models is out of the scope of this paper.

F. Numerical Evaluation Issues

Transcendental equations (7), (19) must be solved numerically. This corresponds to the numerical computation of the roots of the generalized function $f(x) = x - \sum_{k=1}^{M} a_k \exp(b_k x)$ for different sets of the generalized coefficients a_k, b_k. Since the function $f(x)$ varies exponentially with respect to x, arithmetic overflow can occur for x away from the root $f(x_0) = 0$ for high input powers. Therefore, a good initial guess of the root is essential. An approximate evaluation of the root is given by [6] for a certain range of input powers. For WDM applications, this range of input powers must be expanded. Once the neighborhood of the root has been identified, the Newton–Raphson method [28, pp. 362–367] is used for root refinement. Newton–Raphson is the method of choice here since it converges quadratically near the root, i.e., the number of significant digits doubles at each iteration.

Integrals (11), (12) are evaluated numerically by use of the Gauss–Legendre method [28, pp. 147–161]. The computation of Eq. (24) can be (arbitrarily) used as a criterion to determine the number of nodes that are necessary for the numerical integration. It is found that ten nodes are sufficient for a relative error in the evaluation of $r(t)$ less than 10^{-4}.

When the EDF model of Refs. [1, 2] is used in the simulation of multiwavelength optical networks, error-monitoring is essential. If the relative error in the evaluation of gain or ASE noise exceeds a certain threshold value, the model should automatically switch to the variant by [12] or the alternative EDF models of [11, 13–17]. As a rule of thumb, the model in Refs. [1, 2] is usually considered reasonably accurate for gains less than 20 dB [4]. This criterion is not strict. It is obvious from relation (16) that when the average powers of the input beams $P_k(z)$, $1 \leq k \leq M$ are large compared to the output ASE noise power at every point z into the fiber, the error must be small even for gains higher than 20 dB.

Finally, the execution time per EDF module increases linearly with the size of the wavelength grid. Nonuniform resolution can be used to reduce the execution time [30, 31] (see Section III below).

III. WAVELENGTH-DOMAIN SIMULATION PRINCIPLES

The EDF model of Section II can be used for the study of the optical transport layer of multiwavelength optical networks. For this purpose, a library of models of other optical devices and components must be developed. These models must be sufficiently fast to enable the study of large-scale networks. There is a trade-off between accuracy of representation and execution speed. Abstract, phenomenological models of the optical signals and network components, not necessarily based on a detailed physical description, are more adequate for network simulations.

To simplify the representation of the optical signals and network components and to reduce the number of numerical operations, it is assumed that the network components do not alter the shape of the signal waveforms, i.e., signal distortion due to linear or nonlinear effects is ignored. Based on the above assumption, the modulation of optical signals is ignored since it is not influenced by the WDM optical network element components. Furthermore, optical signals are represented by their carrier wavelength and average power exclusively and not by their temporal waveform, as is customary in simulation of analog and digital communication systems [19].

For the computer representation of the optical signals, the wavelength axis is discretized into N wavelength bins. The choice of the wavelength bin size is arbitrary and depends on the desired accuracy (see below). Typically, the wavelength bin size is several times the bit-rate. The central wavelengths of these wavelength bins define a grid.

The representation of the optical signals differs depending on whether or not they occupy one or several wavelength bins (defined as narrowband or wideband optical signals, respectively). We distinguish two different types of optical signals, namely, optical signals produced by laser sources (narrowband) and ASE noise (wideband). Each type is represented separately. (1) Optical signals produced by laser sources are represented by a pair of numbers (carrier wavelength, average power). (2) Forward and backward ASE noises are represented by $N \times 2$ matrices (i.e., N pairs of numbers (wavelength node, average ASE power at this node of the wavelength grid)).

The above representation can be extended to include, for each optical signal, all interfering terms originating from the same laser source as the signal and recombining with it after propagation through different optical paths (i.e., multipath optical crosstalk) [18]. Since the modulation, phase, and polarization of all optical signals are ignored in the wavelength-domain, it is not correct to simply add the average power of each signal and its corresponding multipath interference. Therefore, for simulation purposes, multipath interferers are represented separately as distinct narrowband optical signals in the same wavelength bin as the optical signal.

For example, Fig. 1a shows the computer representation of an optical signal produced by a laser source contaminated by ASE noise and six multipath interferers. Without loss of generality, only five nodes of the wavelength grid are shown. All signal power is concentrated into the third wavelength bin (black column). ASE noise power is distributed into all five wavelength bins (white columns). The six multipath interferers, denoted by Px_1–Px_6, are represented by distinct gray columns in the same wavelength bin as the optical signal.

A WDM signal composed of M individual optical signals is represented in the wavelength-domain by a set of M graphs similar to Fig. 1a, one for each different laser source.

An example of transmittance transfer function of an optical component (e.g., optical filter) is shown in Fig. 1b. Similar to Fig. 1a, only five nodes of the wavelength grid are shown. The transmittance transfer functions are described by $N \times 2$ matrices (i.e., N pairs of numbers (wavelength, values of the gain/loss at the nodes of the grid)). These can be given either by an analytical relationship or as a table of measured values. The gain or loss is assumed to be approximately constant within a single wavelength bin but may be different for signals at adjacent wavelength bins. The gain or loss may also vary as a function of time but this variation is slow compared to the bit period (quasistatic components). The phase transfer functions of the network components are discarded.

As optical signals, ASE noise, and optical crosstalk pass from one module to the other, their average powers at the N grid nodes are multiplied by the corresponding values of the gain/loss of the modules. It is thus possible to evaluate the average powers of optical signal, ASE noise, and optical crosstalk at every point of the network.

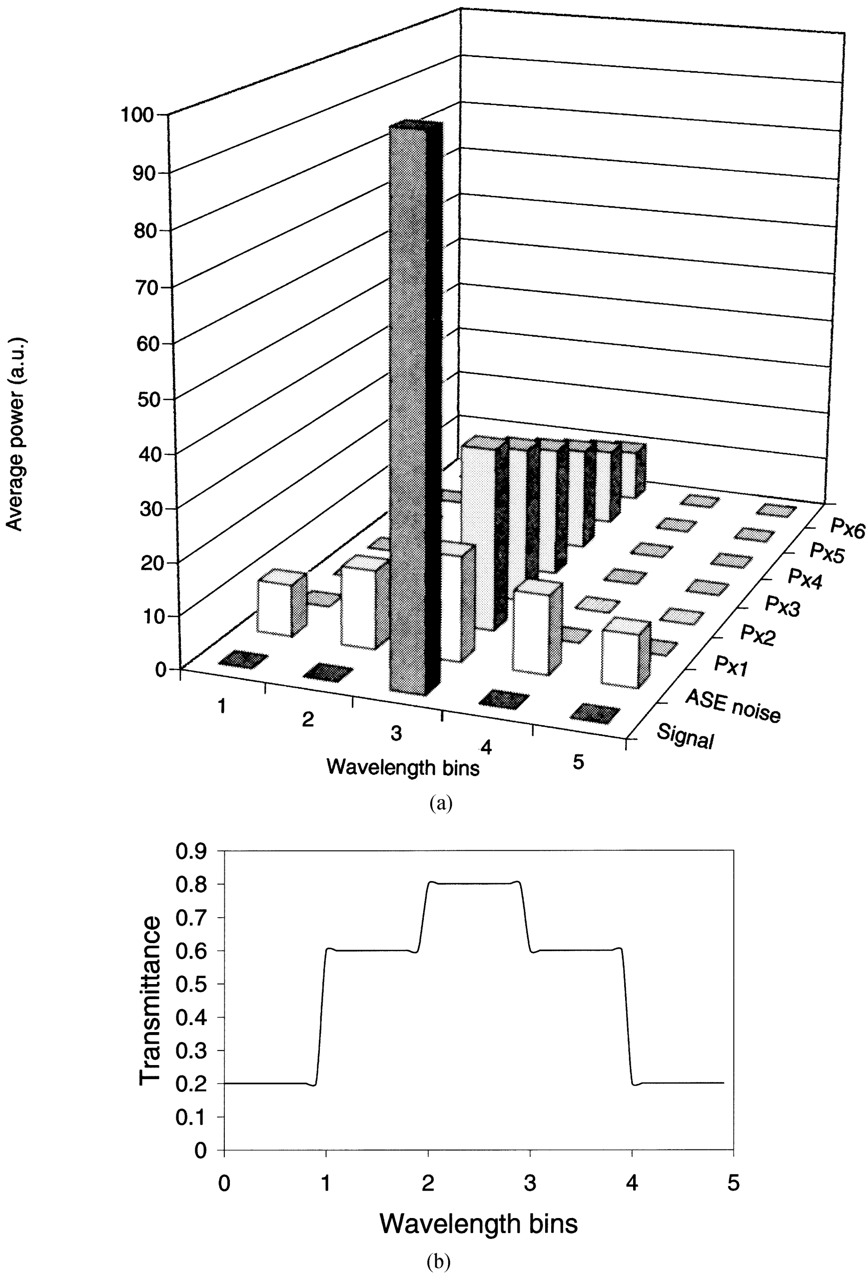

FIG. 1. (a) Wavelength-domain representation of an optical signal produced by a laser source contaminated by ASE noise and six multipath interferers. (Symbols: signal, black column; ASE noise, white columns; multipath interferers, Px_1–Px_6, gray columns). (b) Transmittance transfer function of an optical component.

In the following, this computer representation is referred to as wavelength-domain representation. It can be used for efficient steady-state and transient optical signal, ASE noise, and optical crosstalk power-budget computations in the optical transport layer of multiwavelength optical networks.

An important issue of the wavelength-domain simulation is the choice of *resolution bandwidth* (i.e., the size of the N wavelength bins). In order to accurately evaluate the gain and ASE spectrum of the EDFAs, wavelength-domain resolution bandwidth must be typically on the order of 0.1–1 nm [4]. Higher resolution provides better precision at the expense of computation time and required storage memory. There are some practical considerations in the choice of resolution bandwidth. For easy visualization, it is convenient to set the size of the wavelength bins larger than the individual signal bandwidth in order to restrict all signal power in one bin. This requirement implies a lower limit to the value of the resolution bandwidth. An upper limit is implied by the requirement that two adjacent optical signals must occupy separate wavelength bins. In practice, a more stringent upper limit is necessary in order to describe in detail the shape of the filtered ASE noise power spectra. Similarly to EDF modeling, it is not necessary to use a uniform bin size in the wavelength-domain. Nonuniform bin size can be used to further reduce memory storage requirements and execution time [30, 31].

Another important issue is the choice of *simulation bandwidth* (i.e., optical bandwidth) because, together with resolution bandwidth, it is related to the number of wavelength bins N that must be simulated. To adequately model ASE noise, the simulation bandwidth should include the spectral range 1450–1650 nm. In addition, since pumps at wavelengths around 980 and 1480 nm are used, some extra bins at the pump wavelengths must be anticipated.

The wavelength-domain representation is advantageous in terms of execution speed compared to the waveform-level representations [19]. Its main disadvantage is that several transmission impairments that result in signal distortion (e.g., chromatic dispersion, nonlinearities, polarization effects, etc.) are not considered here. There are several commercial simulation software tools taking into account the above transmission impairments (e.g., OPALS and GOLD [35], BNeD [36], HP EEsof [37], OptSim [38], FOCUSS [39, 40], COMSIS [41], LinkSIM [42]).

Simulation tools based on the wavelength-domain representation can be implemented in a variety of ways. Desirable features of such implementations for the study of different optical transport layer topologies include user-friendliness (e.g., graphic user input and output interfaces, minimum programming), modularity, hierarchical organization, etc. For the MONET project [20], the wavelength-domain simulation tool was implemented using Signal Processing Worksystem (SPW) [43], a communication-systems-oriented commercial software product, as a simulation environment.

Figure 2 shows the organization of the optical library of the MONET wavelength-domain simulation tool. An indicative list of modules is given on the right side in Fig. 2. The modules of the optical library are divided into three hierarchical categories, namely network elements, network element components, and elementary units. Each module is implemented using different designs, technologies, and simulation models and can have uni- or bidirectional fiber interfaces, steady-state

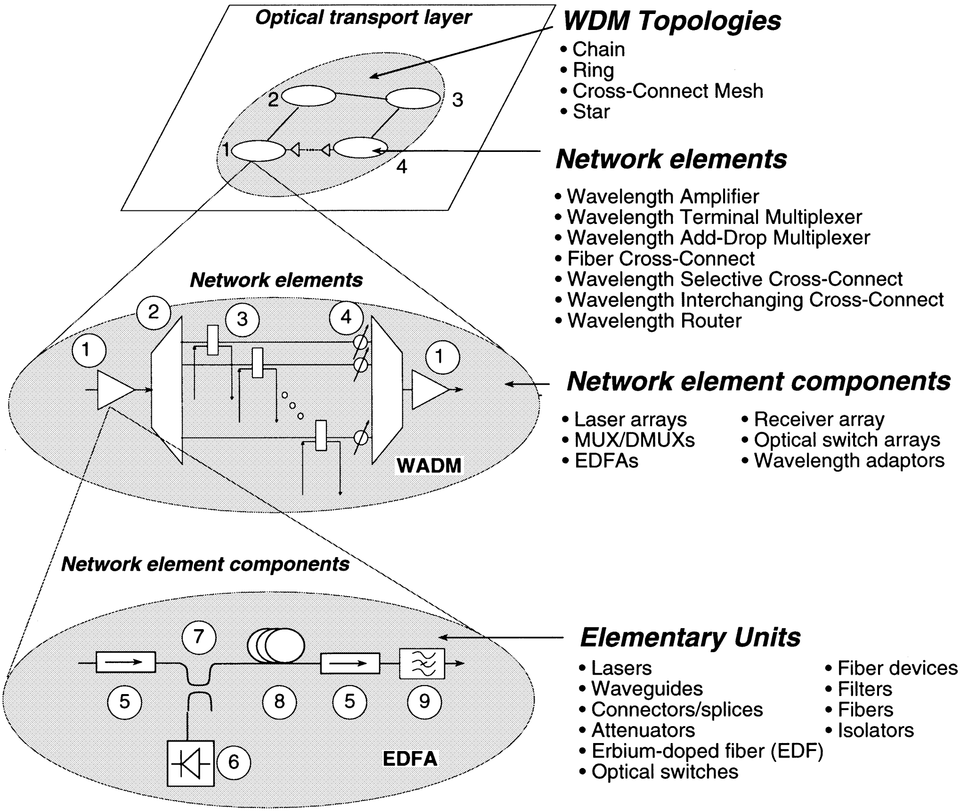

FIG. 2. Schematic overview of the MONET optical transport layer simulation tool. The right column shows an indicative list of WDM topologies, network elements, network element components, and elementary units. On the top left the block diagram of a bidirectional four WADM ring is shown. In the insets, the layouts of a simplified wavelength add–drop multiplexer (WADM) and of a single-stage forward-pumped (EDFA) are shown, respectively. (Symbols: (1) EDFAs, (2) MUX/DMUX, (3) optical 2×2 switches, (4) variable attenuators for power equalization, (5) optical isolator, (6) laser diode, (7) WSC, (8) EDF, (9) ASE rejection filter).

or dynamic properties, and so forth. Modules can be combined in any order to simulate various WDM network topologies. A modeling example is shown on the left side of Fig. 2 and is discussed in greater detail in Section IV.

The MONET wavelength-domain simulation tool was used in the past to study automatic gain control in EDFAs and EDFA chains [44], network topologies [45, 46], and network functionalities [47]. To further illustrate the capabilities of the MONET wavelength-domain simulation tool, an additional example of use is presented below.

IV. SIMULATION EXAMPLE

Power transients due to network reconfiguration, failures, protection switching, etc. are among the most important effects in multiwavelength optical networks that can be studied efficiently using wavelength-domain simulation. Power transients occur at time scales typically in the range of μs−s so the use of conventional waveform-level simulation is impractical. This section presents a brief theoretical study of the transient power fluctuations in a bidirectional wavelength add−drop multiplexer ring.

A. Network Description

Multiwavelength self-healing rings composed of wavelength add−drop multiplexers (WADM) have been proposed as efficient fiber sharing network architectures (see, for example, [48] and the references therein).

The bidirectional four WADM ring topology under study is shown on the top left of Fig. 2. The network elements are represented by circles numbered 1−4. 1 + 1 path protection is assumed [49]. For simplicity, only the equipment in one direction of propagation is shown (e.g., clockwise). At the next hierarchical level, the architecture of a simplified wavelength add-drop multiplexer [20] is shown. The depicted WADM consists of two EDFAs (1), a multiplexer/demultiplexer (MUX/DMUX) pair (2), 2×2 optical switches for signal adding/dropping (3), and servo-controlled attenuators for power equalization (4). At the lowest hierarchical level, the structure of the EDFAs is shown. In this particular example, the EDFAs are identical single-stage forward-pumped amplifiers composed of two isolators (5), a laser diode (6), a wavelength selective coupler (WSC) (7), and a strand of EDF (8).

Due to the nonuniform spectral response of the network element components in the ring and to the fact that signals do not originate at the same point, different channels experience different gains/losses and have different power and optical SNRs at their receivers [50]. The role of the servo-controlled attenuators is to prevent the accumulation of average power and optical SNR spread between channels [51].

Network reconfiguration, failures, protection switching, etc. may cause abrupt changes of the power levels at the input of the servo-controlled attenuators. Depending on their design, servo-controlled attenuators can exhibit transient oscillations before reaching the equilibrium. Transient oscillations caused by power variations of one wavelength channel can be coupled to other wavelength channels due to the cross-saturation effect of the EDFAs. This mechanism is responsible for sustained power fluctuations observed experimentally in large scale networks with closed loops [52].

For the study of transient power fluctuations, a generalized theoretical model of the servo-controlled attenuators is derived and validated experimentally. Using this model, it is shown that the network transient response depends on the magnitude of the initial optical power perturbation, the speed of servo-controlled attenuators, the design of EDFAs, the network topology, and the add/drop scenario. Elimination of the coupling of transients between wavelength channels can be achieved using gain-clamped EDFAs or fast servo-controlled attenuators.

B. Servo-controlled Attenuator Model

Different technologies and designs can be used for the implementation of servo-controlled attenuators (e.g. [53–62]). An exhaustive study of servo-controlled attenuator circuitries is beyond the scope of this paper. A generalized model that captures the essential features of the servo-controlled attenuator's behavior is assumed (Fig. 3).

The generalized model is composed of an optical tap (TAP), a photodetector (P), a lowpass electronic filter (LPF), a comparator (CMP), a control mechanism (CM), and a variable optical attenuator (VOA). A small portion of the light at the output of the variable optical attenuator is tapped and detected by the photodiode. The photodiode is followed by a lowpass filter that eliminates fast power variations. The signal at the output of the lowpass filter is compared with a reference value (REF). The resulting error signal is used to drive the variable optical attenuator through a control mechanism.

For simulation purposes, the control mechanism is modeled by a gain K and the variable optical attenuator is modeled by an integrator. This representation stems from the (arbitrary) assumption that the rate of change of the attenuation is a linear function of the error signal $e(t)$ at the output of the comparator; i.e., $da(t)/dt = Ke(t)$. It is worth noting that K is related to the speed of the attenuator. The above relationship can be rewritten in the more eloquent integral form $a(t) = \int_{-\infty}^{t} Ke(t')\,dt'$ which indicates that, only when there is a nonzero error signal, the value of the attenuation changes. In the absence of an error signal, the variable optical attenuator maintains its previous value. The ends of the attenuation range are set by upper and lower limit parameters. When the integration result would otherwise exceed the upper limit or fall below the lower limit, the output is set equal to the upper-limit or lower-limit value.

The step response of the servo-controlled attenuator model is derived in the Appendix, assuming that the lowpass filter is modeled as a finite time integrator with impulse response of duration τ. It is shown that the step response of the servo-controlled attenuator depends on the choice of the design parameters K and τ and on the level of the input power jump. Different combinations of the above

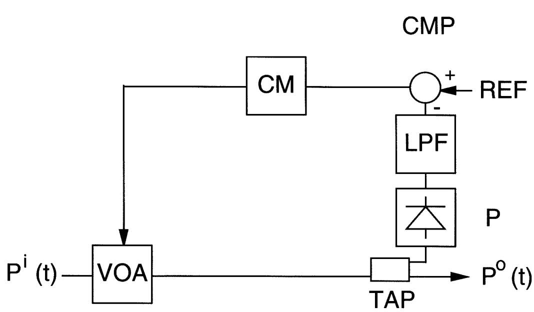

FIG. 3. Block diagram of a generalized servo-controlled attenuator. (Symbols: TAP, optical tap; P, photodetector; LPF, lowpass electronic filter; CMP, comparator; REF, reference signal; CM, control mechanism; VOA, variable optical attenuator).

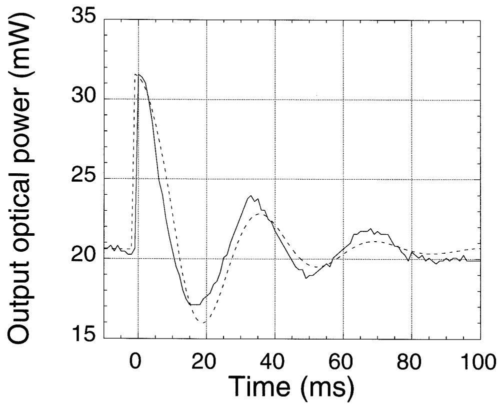

FIG. 4. Step response of a commercial servo-controlled attenuator (Solid line, experiment; broken line, simulation).

quantities result in completely different behavior of the output power that varies from exponentially damped to underdamped oscillations and clipping, when the ends of the attenuation range are reached.

To test the validity of the servo-controlled attenuator model, measurements of the step response of a commercially available opto-mechanical servo-controlled attenuator are compared with simulation results below.

Figure 4 shows the measured (solid line) and the simulated (broken line) optical power at the output of the servo-controlled attenuator when the input power is suddenly increased by 3 dB at the time instant $t = 0$. The overshoot of the output power is instantaneous. After the overshoot, the output power oscillates and eventually reaches a constant reference value. Although not visible in the time scale of the graph, it is found that the oscillation frequency decreases gradually during the step as the output power approaches the equilibrium value. It is also observed that the level of the discontinuity and the oscillation frequency vary for different input power jumps. Despite the simplicity of the theoretical model, there is a good qualitative agreement between theory and experiment. This result justifies the use of the generated servo-controlled attenuator model for the study of the transient response of multiwavelength optical networks.

C. Other Modules

The servo-controlled attenuators used in the WADM ring under study are assumed to respond much more slowly to changes in input power than the EDFA gain. Therefore, in the simulation the static spectrally resolved EDF model by Saleh, Jopson et al. [1, 2] is used.[1] In reality, the output power variations consist of

[1] For a recent experimental validation of the static spectrally resolved EDF model by Saleh, Jopson et al. [1, 2], the interested reader is referred to [63].

a fast component due to EDFA response that decays in a time scale on the order of millisecond and a slow component due to the attenuator response that is assumed to last for several tens of milliseconds. The results of the following section do not include the fast component due to EDFA response.

Different technologies can be used for the implementation of MUX/DMUXs depending on the specifications of insertion loss, bandwidth, passband shape, passband ripple, stopband response, and other considerations. In this example, the MUX/DMUX are hierarchical blocks composed of elementary optical filters in parallel. The transmittance transfer functions of the elementary optical filters are assumed identical and have ideal rectangular shape (i.e., uniform insertion loss within the passband and perfectly opaque stopbands).

The 2×2 optical switches are characterized exclusively by their state and insertion loss. The switching speed is not taken into account.

The numerical values of the parameters used in the simulation are the following: Fiber links between WADMs 1–4 are assumed to have 21 dB flat attenuation (i.e., the fiber length is assumed 60 km with attenuation 0.35 dB/km). The length of the fiber link between the fourth and the first WADM is assumed 3000 km. It consists of 50 fiber spans of 60 km length each. Forty nine EDFAs are used to amplify the optical signals between fiber spans. A single-stage EDFA model is used that provides approximately flat gain 21.7 dB/channel when the input power is -8 dBm/channel. The MUX/DMUX elementary filters bandwidth is 100 GHz. The insertion loss of a MUX/DMUX pair is 10 dB per channel. The optical 2×2 switches are assumed to have 3 dB insertion loss/channel. The servo-controlled attenuators are set to equalize the signal power at a reference value -8 dBm per channel at the input of the power booster EDFA in each WADM. The insertion loss of the servo-controlled attenuators is 2 dB. They are operated at 6 dB additional attenuation. The servo-controlled attenuator design parameters K and τ are chosen so that the output power presents slightly oscillatory behavior for a 3 dB change of the input power level, similar to the commercially available opto-mechanical servo-controlled attenuator of Fig. 4.

All modules are unidirectional, assuming there is strong optical isolation between blocks. Reflections and backward propagating ASE noise are completely eliminated. Transmission impairments are neglected. The information provided by the wavelength-domain representation on optical crosstalk is not taken into account.

The following add–drop scenario is studied: Without loss of generality, it is assumed that only two channels are present at the MONET wavelengths 1549.315 and 1550.918 nm, respectively (200 GHz spacing). Wavelength channel 1 is used to establish a duplex connection between the first and the third WADM. Wavelength channel 2 is used to establish a duplex connection between the second and the fourth WADM. It is assumed that all wavelength channels are added at $t \to -\infty$ so that the network has reached equilibrium at $t \to 0^-$. It is also assumed that the power of wavelength channel 1 in the first WADM is increased or decreased suddenly by 3 dB at the instant $t = 0$.

D. Results and Discussion

Figures 5a and 5b show the output powers of wavelength channels 1 and 2, respectively, at the output of the first and fourth WADMs for a 3 dB rise in the power of channel 1 at the WADM 1. For $t < 0$, the optical power at the output of all WADMs is a constant 13.7 dBm/channel. At the instant $t = 0$, the optical power at the output of the servo-controlled attenuator corresponding to wavelength channel 1 in the first WADM instantaneously increases and then oscillates with decreasing amplitude around its initial value. After the WDM signal passes through the power booster EDFA of the first WADM, power variations in channel 1 induce complementary power variations in channel 2 (solid lines). In the second WADM, channel 2 is dropped and a new channel at the same wavelength is added. After the WDM signal passes through the power booster EDFA of the second WADM, power variations in channel 1 induce complementary power variations in the newly added channel 2. This procedure is repeated in the subsequent WADMs. In each WADM, one of the two channels is dropped and a new channel at the

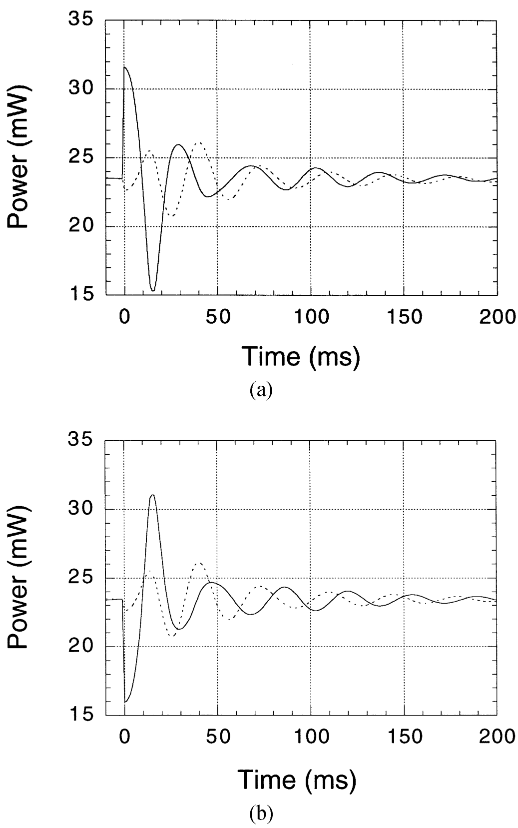

FIG. 5. Optical power fluctuations at the output of the first and fourth WADMs of the bidirectional ring (Fig. 2) due to a 3 dB rise of the power of channel 1 at the WADM 1. (a) Channel 1; (b) channel 2 (Solid line, first WADM; broken line, fourth WADM).

same wavelength is added. Each new added channel is physically disjointed from channel 1 where the initial perturbation occurs. However, the power transient of channel 1 is transferred to the new channel through the complementary power transients acquired by the other channel which is not dropped. After the WDM signal passes through the four WADMs, the magnitude of the discontinuity decreases and the oscillation frequency increases (broken lines). Between the fourth and the first WADM, the propagation delay of the power perturbation is assumed 15 ms. Due to the delay in the feedback loop, the duration of the settling time is about 30% longer than in the case of an individual servo-controlled attenuator. It is worth noting that polarization effects are not considered here.

Similar results are shown in Figs. 6a and 6b for the output powers of wavelength channels 1 and 2, respectively, at the output of the first and fourth WADMs for a 3 dB drop in the power of channel 1 at the WADM 1. The small jump at the solid curves at the instant 15 ms is caused by the feedback.

These results indicate that the cascade of N WADMs is equivalent to $2N$ oscillators (i.e., servo-controlled attenuators) coupled at $2N$ nodes (i.e., EDFAs). This system has modes of oscillation which can be excited through different

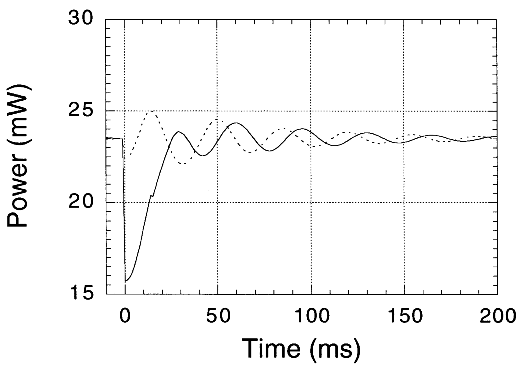

(a)

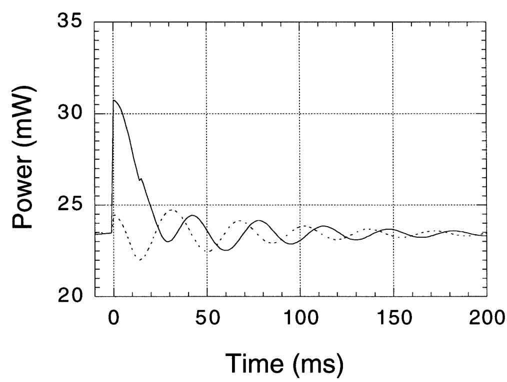

(b)

FIG. 6. Same as Fig. 5 for a 3 dB drop of the power of channel 1 at the WADM 1.

add−drop scenarios[2]. The result is a progressive wave (i.e., power perturbation) that propagates in the network. If closed loops of sufficient length exist, standing waves can be formed depending on the propagation delay. Therefore, the servo-controlled attenuators and the EDFAs must be properly designed in order for the oscillations to be damped.

To avoid coupling of power variations from one channel to other channels, the use of gain-clamped amplifiers was proposed [52]. Preliminary simulations show that the coupling between wavelength channels will be negligible or very small in this case. Only the wavelength channel that experienced the initial perturbation is affected. For this channel, the perturbation evolves as it propagates through a transparent chain of cascaded network elements.

Another solution for avoiding coupling of power variations from one channel to other channels is to use servo-controlled attenuators which respond much faster to changes in input power than the EDFA gain. Again, only the wavelength channel that experienced the initial perturbation is affected.

In the above example, 57 EDFAs are used in the ring. If the sampling interval is 1 ms, the total number of calls to the erbium-doped fiber function for the 200 ms window shown in Figs. 5 and 6 exceeds 11,000. This fact shows the importance of the choice of the EDF model and of the wavelength-domain representation. For simulation of larger and more complex networks, even the efficient spectrally resolved EDF model by Saleh, Jopson et al. [1, 2] might be inadequate and a simpler black-box model like, e.g., [16, 17] might be necessary.

V. SUMMARY

A growing trend in the optical communications field is the ability to model large-scale multiwavelength optical networks. The size and complexity of these networks impose limitations in execution speed and raise the need of efficient modeling approximations. The adequate choice of the model of EDFAs and of the computer representation of the optical signals and other network components are discussed here.

The first part of this paper reviews the spectrally resolved erbium-doped fiber model by Saleh, Jopson et al. [1, 2]. The second part of this paper reviews the wavelength-domain representation of optical signals and systems at the optical transport layer of multiwavelength optical networks. As a simulation example, transient power fluctuations caused by the dynamic interaction of servo-controlled attenuators and saturated erbium-doped fiber amplifiers in a bidirectional ring of wavelength add−drop multiplexers are studied. The mechanism responsible for this oscillatory behavior are identified and remedies are proposed.

[2] The use of the term “mode” here is not strict. According to the conventional definition found in the context of linear oscillating systems [64, chap. 6], normal modes correspond to constant oscillation frequencies, identical for all oscillators. The servo-controlled attenuator is not a linear component. Its oscillation frequency depends on the power level at its input and the step response is slightly chirped (see Appendix).

APPENDIX

Servo-controlled Attenuator Step Response

This Appendix provides an analytical derivation of the step response of the servo-controlled attenuator model of Fig. 3.

To simplify the analysis, we limit our interest in the case where the variable optical attenuator does not reach the ends of its position range (i.e., $a_{min} < a(t) < a_{max}$). In this case, the variable optical attenuator is modeled as an ideal integrator. For mathematical convenience, several additional simplifications are made: (i) It is assumed that all output power is detected by the photodiode. In practice, the tap scales the signal incident at the photodiode, but the scaling factor is included in the gain coefficient K. (ii) Similarly, the photodiode is omitted since it only makes a linear conversion from total output power to current (assuming that the responsivity is constant for the wavelength range under study). The responsivity is included in the gain coefficient K. As a result, all signals in the control circuit are expressed in units of power except for the signal from the control mechanism to the variable optical attenuator, which has no units. The gain coefficient K is expressed in units of inverse power. (iii) The optical signal noise and the thermal noise of the receiver and the electronic circuit are neglected. (iv) The lowpass filter is modeled as a finite time integrator with impulse response

$$h(t) = \begin{cases} \dfrac{1}{\tau} & 0 \leq t \leq \tau \\ 0 & \text{elsewhere}. \end{cases} \tag{25}$$

The input and output total powers are denoted by $P^i(t)$, $P^o(t)$, respectively. The reference power is denoted by P_r.

The servo-controlled attenuator is described by an integrodifferential equation:

$$\frac{da(t)}{dt} = K\left[P_r - \frac{1}{\tau}\int_{t-\tau}^{t} a(t')P^i(t')\,dt'\right]. \tag{26}$$

Differentiating again each member of (26) yields

$$\frac{d^2a(t)}{dt^2} = \frac{K}{\tau}\left[-a(t)P^i(t) + a(t-\tau)P^i(t-\tau)\right]. \tag{27}$$

A step signal is applied at the input

$$P^i(t) = \begin{cases} P_1 & t \geq 0 \\ P_0 & t < 0. \end{cases} \tag{28}$$

It is assumed that $a(0) = a_0$ and that the attenuator has reached the equilibrium for $t \to 0^-$ so $a_0 P_0 = P_r$. In addition, it is assumed that the $da(0)/dt \simeq 0$. The last condition implies that the integral $I(t) = (1/\tau)\int_{t-\tau}^{t} a(t')P^i(t')\,dt'$ in (26) does not change significantly at $t = 0$ due to the discontinuity of the input signal and so $I(0) \simeq a_0 P_0 = P_r$.

Due to the term $a(t-\tau)P^i(t-\tau)$, the delay differential equation (27) has a different form at different time intervals. Equation (27) can be solved using various methods (e.g., see [65] and the references therein). However, the analytic solution is cumbersome and is given here only at the time intervals $[0,\tau)$, $[\tau, 2\tau)$.

The attenuation in the interval $[0,\tau)$ is given by

$$a(t) = \left(a_0 - \frac{P_r}{P_1}\right)\cos \omega t + \frac{P_r}{P_1}, \tag{29}$$

where $\omega = \sqrt{KP_1/\tau}$.

Relation (29) describes a simple harmonic motion with angular oscillation frequency ω. This oscillation lasts only for a time period τ. Then the feedback acts as a force that can damp the oscillatory behavior. For $t \in [\tau, 2\tau)$ the attenuation is given by

$$a(t) = \frac{1}{4}\left(a_0 - \frac{P_r}{P_1}\right)[3\cos(\omega t) + \cos \omega(t-2\tau) + 2\omega(t-\tau)\sin \omega(t-2\tau)] + \frac{P_r}{P_1}. \tag{30}$$

The output power is given by

$$P^o(t) = \begin{cases} (a_0 P_1 - P_r)\cos \omega t + P_r & t \in [0,\tau) \\ \frac{1}{4}(a_0 P_1 - P_r)[3\cos(\omega t) + \cos \omega(t-2\tau) & \\ \qquad + 2\omega(t-\tau)\sin \omega(t-2\tau)] + P_r & t \in [\tau, 2\tau). \end{cases} \tag{31}$$

As a special case, assume that the bandwidth of the lowpass filter is very large compared to the bandwidth of the output signal power variations (i.e., the filtering time $\tau \to 0$). Then, the integrodifferential equation (26) is reduced to a first-order ordinary differential equation:

$$\frac{da(t)}{dt} = K\left[P_r - a(t)P^i(t)\right]. \tag{32}$$

The attenuation is given by

$$a(t) = \left(a_0 - \frac{P_r}{P_1}\right)e^{-KP_1 t} + \frac{P_r}{P_1}. \tag{33}$$

The output power is given by

$$P^o(t) = (a_0 P_1 - P_r)e^{-KP_1 t} + P_r. \tag{34}$$

The following observations can be drawn:

- For narrowband LPF, the output power jumps instantaneously at $t = 0$ by $a_0|P_1 - P_0|$ and then exhibits oscillations around the position of equilibrium P_r.

The oscillation frequency depends uniquely on K, P_1, and τ. It increases with the increase of K, P_1 and decreases with the increase of τ. Consequently, the oscillation frequency is larger for power rises than for power drops by the same amount. In addition, it can be shown that the settling time of the relaxation oscillations is longer when K, P_1, and τ increase.

- For wideband LPF, no oscillations are observed. The jump in output power is instantaneous at $t = 0$. The level of the discontinuity is $a_0|P_1 - P_0|$. The output power after the jump decreases or increases exponentially with a time constant $1/(KP_1)$ to the reference value P_r, depending on if $P_1 > P_0$ or $P_1 < P_0$, respectively. Since the time constant is dependent on the input signal power, a rise and a drop by the same amount in the input power are not characterized by the same time constant.

To study the step response of more realistic lowpass (e.g., Butterworth) filters or the effect of clipping, numerical solution of the delay differential equation (27) is required (see, for example, [66] and the references therein).

VI. ACKNOWLEDGEMENTS

The authors are grateful to Drs. E. Desurvire, A. F. Elrefaie, J. L. Zyskind, R. E. Tench, E. L. Goldstein, and J. Y. Pan for their encouragement, help, remarks and suggestions; to Drs. Y. Sun, A. Bononi, M. Nissov, and M. Gunkel for recommending the references [9], [11], [12], [16], [17]; to Ms. J. E. Baran for providing the measurements of Fig. 4; and to Ms. L. M. Szemiot for corrections in the syntax of the manuscript.

REFERENCES

1. A. A. M. Saleh, R. M. Jopson, J. D. Evankow, and J. Aspell, "Modeling of gain in erbium-doped fiber amplifiers," *IEEE Photon Technol. Lett.*, vol. 2, 714 (1990).
2. R. M. Jopson and A. A. M. Saleh, "Modeling of gain and noise in erbium-doped fiber amplifiers," in *Fiber Laser Sources and Amplifiers III*, vol. 1851, pp. 114–119, SPIE, 1991.
3. E. Desurvire, *Erbium-doped fiber amplifiers: Principles and applications*. Wiley, New York, 1994.
4. C. R. Giles and E. Desurvire, "Modeling erbium-doped fiber amplifiers," *J. Lightwave Technol.*, vol. 9, 271 (1991).
5. T. Pfeiffer and H. Bülow, "Analytical gain equation for erbium-doped fiber amplifiers including mode field profiles and dopant distribution," *IEEE Photon Technol. Lett.*, vol. 4, 449 (1992).
6. E. Desurvire, "An explicit analytical solution for the transcendental equation describing saturated erbium-doped fiber amplifiers," *Opt. Fiber Technol.*, vol. 2, no. 4, 367 (1996).
7. Y. Sun, J. L. Zyskind, and A. K. Srivastava, "Average inversion level, modeling and physics of erbium-doped fiber amplifiers," *IEEE J. Select. Topics Quantum Electron.*, vol. 3, 991 (1997).
8. Y. Sun, G. Luo, J. L. Zyskind, A. A. M. Saleh, A. K. Srivastava, and J. W. Sulhoff, "Model for gain dynamics in erbium-doped fiber amplifiers," *El. Lett.*, vol. 32, 1490 (1996).
9. Y. Sun, A. A. M. Saleh, J. L. Zyskind, D. L. Wilson, A. K. Srivastava, and J. W. Sulhoff, "Time dependent perturbation theory and tones in cascaded erbium-doped fiber amplifier systems," *J. Lightwave Technol.*, vol. 15, 1083 (1997).

10. A. Bononi and L. A. Rusch, ''Doped fiber amplifier dynamics: a system perspective,'' *J. Lightwave Technol.*, vol. 16, 945 (1998).

11. L. Tančevski, A. Bononi, and L. A. Rusch, ''Output power and SNR swings in cascades of EDFAs for circuit- and packet-switching optical networks.'' submitted for publication.

12. M. Nissov, ''Extension of semi-analytical erbium-doped fiber amplifier model to self-saturation regime,'' *Opt. Fiber Technol.*, vol. 3, 134–141 (1997).

13. T. Georges and E. Delevaque, ''Analytic modeling of high-gain erbium-doped fiber amplifiers,'' *Opt. Lett.*, vol. 17, 1113 (1992).

14. T. G. Hodgkinson, ''Average power analysis technique for erbium-doped fiber amplifiers,'' *IEEE Photon Technol. Lett.*, vol. 3, 1082 (1991).

15. T. G. Hodgkinson, ''Improved average power analysis technique for erbium-doped fiber amplifiers,'' *IEEE Photon Technol. Lett.*, vol. 4, 1273 (1992).

16. D. Bonnedal, ''EDFA gain described with a black box model, in *OSA Trends in Optics and Photonics, Vol. 5, Optical Amplifiers and Their Applications*, pp. 53–56 (1996).

17. J. Burgmeier, A. Cords, R. März, C. Scäffer, and B. Stummer, ''A black box model of EDFA's operating in WDM systems,'' *J. Lightwave Technol.*, vol. 16, 1271 (1998).

18. I. Roudas, N. Antoniades, R. E. Wagner, S. F. Habiby, T. E. Stern, and A. F. Elrefaie, ''Wavelength-domain simulation of linear multiwavelength optical networks,'' submitted.

19. K. S. Shanmugan, ''Simulation and implementation tools for signal processing and communication systems,'' *IEEE Comm. Mag.*, 36 (Jul. 1994).

20. R. E. Wagner, R. C. Alferness, A. A. M. Saleh, and M. S. Goodman, ''MONET: Multiwavelength optical networking,'' *J. Lightwave Technol.*, vol. 14, 1349 (1996).

21. H. Masuda, A. Takada, and K. Aida, ''Modeling the gain degradation of high-concentration erbium-doped fiber amplifiers by introducing inhomogeneous cooperative up-conversion,'' *J. Lightwave Technol.*, vol. 10, 1789 (1992).

22. P. Myslinski, D. Nguyen, and J. Chrostowski, ''Effects of concentration on the performance of erbium-doped fiber amplifiers,'' *J. Lightwave Technol.*, vol. 15, 112 (1997).

23. F. W. Willems, ''Analytic approximation of amplified signal double Rayleigh scattering in pumped erbium doped fibres,'' *El. Lett.*, vol. 33, 49 (1997).

24. P. F. Wysocki, G. Jacobovitzveselka, D. S. Gasper, S. Kosinski, J. Costelloe, and S. W. Granlund, ''Modeling, measurement, and a simple analytic approximation for the return loss of erbium-doped fiber amplifiers,'' *IEEE Photon Technol. Lett.*, vol. 7, 1409 (1995).

25. M. N. Zervas and R. I. Laming, ''Rayleigh-scattering effect on the gain efficiency and noise of erbium-doped fiber amplifiers,'' *IEEE J. Quantum Electron.*, vol. 31, 468 (1995).

26. L. J. Wang, J. T. Lin, and P. Ye, ''Analysis of polarization dependent gain in fiber amplifiers,'' *IEEE J. Quantum Electron.*, vol. 34, 413 (1998).

27. J. L. Wagner, D. G. Falquier, M. J. F. Digonnet, and H. J. Shaw, ''A Mueller matrix formalism for modeling polarization effects in erbium-doped fibers,'' *J. Lightwave Technol.*, vol. 16, 200 (1998).

28. W. Press, B. Flannery, S. Teukolsky, and W. Vetterling, *Numerical Recipes in C: The Art of Scientific Computing*, 2d ed., Cambridge Univ. Press, Cambridge, UK, 192.

29. J. H. Povlsen, A. Bjarklev, O. Lumholt, H. Vendeltorp-Pommer, K. Rottwitt, and T. P. Rasmussen,''Optimizing gain and noise performance of EDFA's with insertion of a filter or an isolator,'' in *Fiber Laser Sources and Amplifiers III*, Boston, MA, M. J. Digonnet and E. Snitzer, Eds., vol. 1581, pp. 107–113, SPIE, Mar. 1991.

30. E. Jaunart, P. Crahay, and B. Heens, ''Efficient tools for EDFA design: an experimental and theoretical analysis,'' in *Fiber Optic Network Components*, Amsterdam, H. Porte and S. I. Najafi, Eds., vol. 249, pp. 224–235, SPIE, Mar. 1995.

31. S. L. Zhang and J. J. O'Reilly, ''EDFA custom-coded simulation block for use in WDM optical fiber communication system studies,'' *Simulation*, vol. 63, 377 (1994).

32. D. Lomen and J. Mark, *Ordinary Differential Equations with Linear Algebra*, Prentice-Hall, New York, 1986.

33. C. Barnard, P. Myslinski, J. Chrowstowski, and M. Kavehrad, "Analytical model for rare-earth-doped fiber amplifiers and lasers," *IEEE J. Quantum Electron.*, vol. 30, 1817 (1994).

34. K. Bertilsson and P. A. Andrekson, "Modeling of noise in erbium-doped fiber amplifiers in the saturated regime," *J. Lightwave Technol.*, vol. 12, 1198 (1994).

35. A. J. Lowery and P. C. R. Gurney, "Two simulators for photonic computer-aided design," *Appl. Opt.*, vol. 37, 6066 (1998). See also http://www.virtualphotonics.com/.

36. "BroadNeD." http://www.virtualphotonics.com/.

37. A. F. Elrefaie, "Computer-aided modeling and simulation of lightwave systems," *IEEE LEOS Newsletter*, vol. 7, 1, (1993).

38. ARTIS, *OptSim*. http://www.artis.it.

39. C. Glingener, J. P. Elbers, and E. Voges, "Simulation tool for WDM networks," in *Colloquium on WDM Technology and Applications,* vol. 1, IEE (1997).

40. ZEDO, "FOCUSS." http://focuss.zedo.fuedo.de.

41. C. Le Brun, E. Guillard, and J. Citerne, "Communication systems interactive software (COMSIS): modeling of components and its application to the simulation of optical communication systems," *Appl. Opt.*, vol. 37, 6059, (1998).

42. RSoft, *LinkSIM*. http://www.rsoftinc.com.

43. Alta group, *Signal Processing Worksystem*, *Version 3.5*. Cadence Design Systems, Inc., Feb. 1996.

44. D. H. Richards, J. L. Jackel, and M. A. Ali, "A theoretical investigation of dynamic all-optical automatic gain control in multichannel EDFA's and EDFA cascades," *IEEE J. Select. Topics Quantum Electron.*, vol. 3, 1027 (1997).

45. N. Antoniades, I. Roudas, R. E. Wagner, and S. F. Habiby, "Simulation of ASE noise accumulation in a wavelength add-drop multiplexer cascade," *IEEE Photon Technol. Lett.*, vol. 9, 1274 (1997).

46. N. Antoniades, I. Roudas, R. E. Wagner, T. E. Stern, J. L. Jackel, and D. H. Richards, "Use of wavelength- and time-domain simulation to study performance degradations due to linear optical crosstalk in WDM networks," *OSA TOPS*, *Opt. Net. Appl.*, vol. 20, 288 (1998).

47. D. H. Richards, J. L. Jackel, I. Roudas, W. Xin, N. Antoniades, and M. Ali, "Method for detecting fiber cuts in a WDM ring with saturated EDFAs," in *Optical Fiber Communication Conference* (*OFC*), San Diego, CA, no. FJ4, OSA, Feb. 1999.

48. A. F. Elrefaie, "Multiwavelength survivable ring network architectures," in *Int. Conf. Comm.* (*ICC*), pp. 1245–1251, IEEE, May 1993.

49. R. Ramaswami and K. N. Sivarajan, *Optical Networks: A Practical Perspective* Morgan Kaufman, San Mateo, CA (1998).

50. A. F. Elrefaie and S. Zaidi, "Fibre amplifiers in closed-ring WDM networks," *El. Lett.*, vol. 28, 2340 (1992).

51. A. F. Elrefaie, E. L. Goldstein, S. Zaidi, and N. Jackman, "Fiber-amplifier cascades with gain equalization in multiwavelength unidirectional inter-office ring networks," *IEEE Photon Technol. Lett.*, vol. 5, 1026 (1993).

52. S. J. B. Yoo, W. Xin, L. D. Garrett, J. C. Young, G. Ellinas, J. C. Chiao, M. Rauch, J. E. Baran, B. Meagher, H. Leblanc, and G. K. Chang, "Observation of prolonged power transients in a reconfigurable multiwavelength network and their suppression by gain-clamping of optical amplifiers," *IEEE Photon Technol. Lett.*, vol. 10, 1659 (1998).

53. S. H. Huang, X. Y. Zou, S. M. Huang, A. E. Willner, Z. Bao, and D. A. Smith, "Experimental demonstration of dynamic network equalization of three 2.5-Gb/s WDM channels over 1000 km using acoustooptic tunable filters," *IEEE Photon Technol. Lett.*, vol. 8, 1243 (1996).

54. J.-X. Cai, K.-M. Feng, X. Chen, A. E. Willner, D. A. Smith, C.-H. Lee, and Y.-J. Chen, "Experimental demonstration of dynamic high-speed equalization of three WDM channels using acoustooptic modulators and a wavelength multiplexer," *IEEE Photon Technol. Lett.*, vol. 9, 678 (1997).

55. D. S. Starodubov, V. Grubsky, A. Skorucak, J. Feinberg, J. X. Cai, K. M. Feng, and A. E. Willner, ''Novel fiber amplitude modulators for dynamic channel power equalization in WDM systems,'' in *Optical Fiber Communication Conference* (*OFC*), San Jose, CA, no. PD8, Feb. 1998.

56. F. Heismann, P. J. Anthony, E. J. Murphy, and T. O. Murphy, ''Fast automatic power control in optical networks,'' in *ECOC*, no. 448, pp. 303–306, IEE, Sept. 1997.

57. B. Barber, C. R. Giles, V. Askyuk, R. Ruel, L. Stulz, and B. Bishop, ''A fiber connectorized MEMS variable optical attenuator,'' *IEEE Photon Technol. Lett.*, vol. 10, 1262 (1998).

58. C. R. Doerr, C. R. Joyner, and L. W. Stulz, ''Integrated WDM dynamic power equalizer with potentially low insertion loss,'' *IEEE Photon Technol. Lett.*, vol. 10, 1443 (1998).

59. J. E. Ford and J. A. Walker, ''Dynamic spectral control equalization using micro-opto-mechanics,'' *IEEE Photon Technol. Lett.*, vol. 10, 1440 (1998).

60. N. A. O'Brien, J. Gordon, H. Mathew, and B. P. Hichwa, ''An electrochromic variable optical attenuator (ECVOA),'' in *Optical Fiber Communication Conference* (*OFC*), San Diego, CA, no. PD26, Feb. 1999.

61. C. R. Doerr, P. Schiffer, L. W. Stulz, M. Capuzzo, E. Laskowski, A. Paunescu, L. Gomez, and J. Gates, ''Compact integrated dynamic wavelength equalizer,'' in *Optical Fiber Communication Conference* (*OFC*), San Diego, CA, no. PD30, Feb. 1999.

62. C. R. Giles, D. Bishop, B. B. W. V. Askyuk, A. Dentai, R. Ruel, and E. Burrows, ''Low-loss channelized WDM spectral equalizer using lightwave micromachines and autonomous power regulation,'' in *Optical Fiber Communication Conference* (*OFC*), San Diego, CA, no. PD31, Feb. 1999.

63. S. Ovadia and C. Lin, ''Performance characteristics and applications of hybrid multichannel AM-VSB/M-QAM video lightwave transmission systems,'' *J. Lightwave Technol.*, vol. 16, 1171 (1998).

64. H. Goldstein, *Classical mechanics*, Addison-Wesley, Reading, MA, 1981.

65. A. C. Tosi, ''Recent advances in the algebraic system theory of delay-differential equations,'' in *Recent theoretical developments in control*, M. J. Gregson, Ed., University of Leicester, pp. 67–127, Institute of Mathematics and its Applications, Sept. 1976.

66. C. T. Baker, C. A. Paul, and D. R. Willé, ''Issues in the numerical solution of evolutionary delay differential equations,'' *Adv. Comput. Math.*, vol. 3, 171 (1995).